

Self-synchronized Grid-forming Control Strategy for DFIG in Offshore Wind Farm Connected to Diode Rectifier Unit-based HVDC System

Han Wu, Tao Wang, Xiang Meng, and Lijian Wu

Abstract—To reduce the cost of offshore wind power generation systems, the configuration of the offshore wind farm employing doubly-fed induction generator (DFIG) connected to the diode rectifier unit-based high-voltage direct current (DRU-HVDC) system has emerged as an attractive solution. The control strategy of the DFIG plays a crucial role in ensuring reliable operation of the offshore wind power generation system due to the uncontrollable nature of the diode rectifier unit (DRU). This paper proposes a self-synchronized grid-forming control strategy for the DFIG in offshore wind farm connected to DRU-HVDC system. Considering the unique power characteristics of the DRU, the proposed strategy constructs a novel power synchronization control loop, which achieves self-synchronization of the DFIGs in offshore wind farm without any communication network. Additionally, the harmonic distortion induced by the natural commutation characteristic of the DRU introduces significant electromagnetic ripples to the DFIG through the stator windings. To mitigate this, an electromagnetic oscillation reduction method based on harmonic current injection is incorporated into the structure of the proposed strategy. Simulation results based on MATLAB/Simulink validate the effectiveness of the proposed strategy and the electromagnetic oscillation reduction method.

Index Terms—Doubly-fed induction generator (DFIG), grid-forming, diode rectifier unit, high-voltage direct current, offshore wind farm.

I. INTRODUCTION

IN recent years, offshore wind power has developed rapidly. By 2030, the installed capacity of offshore wind power is expected to exceed 380 GW [1]. However, as nearshore areas have been massively developed, the industry is now expanding into deep-sea regions [2].

Currently, the outputs of deep-sea wind projects such as DolWin1 in Germany [3] and Rudong project in China [4] are primarily transmitted via modular multilevel converter-based high-voltage direct current (MMC-HVDC) systems,

which are costly due to their complex power electronics topology and the large-volume offshore platform [5]. Hence, researchers are seeking cost-effective and reliable alternatives for deep-sea wind projects [6]. To reduce the capacity and cost of the MMC, several MMC and diode rectifier unit (DRU) hybrid strategies have been proposed [7]–[11], where the majority of power is transmitted through the DRU. In these strategies, the MMC and DRU are connected in parallel or series on both AC and DC sides, each with its own advantages and disadvantages. However, it is important to note that the voltage and frequency of the offshore AC system are still supported by the MMC, and the stable operation depends on the reliability of the MMC [12]. Moreover, the cost of the MMC remains a concern.

To address the above issues, DRU-based high-voltage direct current (DRU-HVDC), due to its high reliability, compact size, and low cost, is proposed and is attracting increasing attention [13]. Different from the MMC-HVDC system, the operation of the uncontrollable DRU-HVDC system requires that the wind turbines connected to DRU-HVDC system operate in the grid-forming mode [14]. In addition, due to the special power-voltage (P - V) characteristic of the DRU, the synchronization mechanism is different from existing virtual synchronous generator (VSG) or standalone controls [15].

Research in recent years has explored the grid-forming control of wind turbines connected to DRU-HVDC system, and the comparison among the different grid-forming control strategies is listed in Table I. A hybrid centralized and distributed grid-forming control method is proposed in [16] and [17]. To obtain the information on the point of common coupling (PCC) and the reference signals for the centralized control, high-speed communication lines are essential. Alternatively, equipping each wind turbine with a global positioning system (GPS) is another approach [18], [19]. In addition, [20] actively regulates the DC-link voltage of the onshore MMC based on frequency information of the offshore AC grid via communication, thereby enabling active power control of the DRU. On this basis, offshore wind turbines can adopt the classical grid-forming control. However, additional communication or GPS equipment increases the system costs, and their potential failures may impact the stable operation of the offshore wind farm.

Manuscript received: February 20, 2025; revised: May 20, 2025; accepted: September 1, 2025. Date of CrossCheck: September 1, 2025. Date of online publication: August 22, 2025.

This work was supported by the National Natural Science Foundation of China (No. 52577071) and the “Pioneer” and “Leading Goose” R&D Program of Zhejiang (No. 2025C01164).

H. Wu, T. Wang (corresponding author), X. Meng, and L. Wu are with the College of Electrical Engineering, Zhejiang University, Hangzhou, China (e-mail: han.wu@zju.edu.cn; wangtaoee@zju.edu.cn; qdmx1439@163.com; ljw@zju.edu.cn).

DOI: 10.35833/MPCE.2025.000148



TABLE I
COMPARISON OF DIFFERENT GRID-FORMING CONTROL STRATEGIES

Control strategy	Characteristic	Communication	For DRU	For DFIG	Advantage	Disadvantage
Centralized control [16], [17]	Centralized AC voltage control; centralized frequency control	Yes	Yes	No	Simple control structure	Increased cost and low reliability due to communication network
FixReF [18], [19]	No AC voltage control; frequency information obtained by GPS	Yes	Yes	Yes	Simple control structure	Increased cost and low reliability due to GPS; unable to establish AC voltage
Distributed phase-locked loop (PLL)-based control [21], [22]	Decentralized AC voltage control; frequency information obtained by PLL	No	Yes	No	Easy to switch between off-grid and grid-connection	Stability risk due to dynamic of PLL
Decentralized reactive power synchronization based control [26]	No AC voltage control; frequency information obtained by Q - f control loop	No	Yes	No	Self-synchronization	Unable to establish AC voltage
P - V / Q - f control [27]	Decentralized AC voltage control; voltage/frequency information obtained by P - V / Q - f control loop	No	Yes	No	Self-synchronization; able to establish AC voltage	P / Q coupling due to self-synchronization mechanism; complex control structure (power-voltage-current loops)
VSG control [33],[34]	Decentralized AC voltage control; frequency information obtained by P - f control loop	No	No	Yes	Self-synchronization; capable of emulating synchronous generator characteristics	Not applicable to DRU-HVDC system
The proposed control	Decentralized rotor-current-based air-gap flux linkage control; frequency information obtained by Q - f control loop	No	Yes	Yes	Self-synchronization; able to establish AC voltage simplified control structure (power-current loops)	Active and reactive power coupling due to self-synchronization mechanism

To avoid the reliance on communication, a distributed PLL-based control is applied to the wind turbines in [21] and [22]. In addition, the q -axis voltage reference is obtained using local PLL and droop-based reactive power loop, while the d -axis voltage reference is obtained by a proportional-integral (PI)-based active power-voltage control to regulate the voltage amplitude of the offshore wind farm (i.e., P - V control loop). Based on the impedance model established in [23], increasing the proportional gain of the P - V control loop can enhance the system stability. Besides, the coupling relationship between active and reactive power control loops is further analyzed in [24], where angle feedforward control is proposed to enhance the power response capability of the wind turbines.

The asymmetric control structure of PLL may induce instability of wind turbines in weak grids [25]. A self-synchronizing grid-forming control strategy without PLL is proposed in [26], where the voltage frequency or angle of the wind turbine is obtained through droop-based reactive power-frequency control (i.e., Q - f control loop). Nevertheless, the amplitude of the voltage of wind turbine is uncontrolled but clamped by the DRU. Based on the strategy in [26], the voltage amplitude control is introduced in [27], whose reference value is generated by the PI-based active power control. Moreover, a black-start strategy for offshore wind farms connected to DRU is presented in [28]. In order to decouple active and reactive power, a consensus-based reactive power observer is designed in [29] to adjust the virtual impedance acting on the voltage control loop. Besides, a Q - θ type control strategy is proposed to achieve adaptive reactive power

allocation among wind turbines in [30]. Similar grid-forming control strategies are applied to a DRU-based low-frequency AC (LFAC) transmission system and a medium-frequency DRU-based HVDC system in [31] and [32], respectively.

In general, the existing research primarily uses permanent magnet synchronous generators (PMSGs) in the offshore wind turbines. With the launch of large-capacity offshore doubly-fed induction generators (DFIGs) by the wind turbine manufacturers, the application of cost-effective DFIG has become another option to reduce the development cost of offshore wind power generation. Hence, the configuration of the grid-forming DFIG-based wind farm connected to the DRU-HVDC system has emerged as an attractive and cost-minimizing solution.

The grid-forming control strategies of DFIGs are extensively investigated in [33], [34]. The grid-support ability and synchronous dynamics of the existing strategies are determined by the droop- or VSG-based P - f and Q - V control loops. However, these grid-forming control strategies cannot be directly applied to the DFIGs connected to the DRU-HVDC system, as their synchronization mechanism does not match the P - V characteristics of the DRU.

Therefore, this paper proposes a self-synchronized grid-forming control strategy for the DFIG in offshore wind farm connected to DRU-HVDC system. The specific contributions can be summarized as follows.

- 1) Based on the self-synchronization mechanism, a self-synchronized grid-forming control strategy is constructed, which achieves self-synchronization of DFIGs.
- 2) Considering the harmonic distortion caused by the

DRU, an electromagnetic oscillation reduction method based on harmonic current injection is incorporated into the structure of the proposed strategy, which is guided by the sensitivity analysis.

The remainder of this paper is organized as follows. Section II presents the mathematical model and self-synchronization mechanism. Section III introduces the proposed strategy. Section IV gives the stability analysis. In Section V, an electromagnetic oscillation reduction method is developed. The simulation verifications are presented in Section VI. Section VII concludes this paper.

II. MATHEMATICAL MODEL AND SELF-SYNCHRONIZATION MECHANISM

The structure of DFIG in offshore wind farm connected to DRU-HVDC system is shown in Fig. 1. Since this paper primarily focuses on the control of DFIG in offshore wind farm connected to DRU-HVDC system, the onshore MMC, which regulates the onshore DC voltage of HVDC, can be simplified as a constant DC voltage source [23]. In addition, the self-synchronization mechanism is also described. In Fig. 1, RSC represents the rotor-side converter; GSC represents the grid-side converter; T_{DFIG} represents the DFIG transformer; and T_{MMC} represents the MMC transformer.

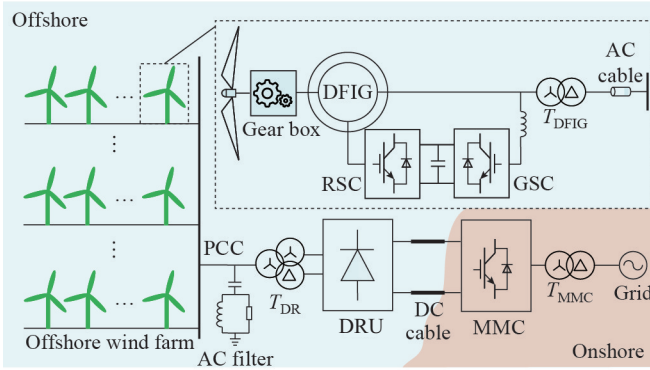


Fig. 1. Structure of DFIG in offshore wind farm connected to DRU-HVDC system.

A. Mathematical Model of DFIG

The equivalent circuit diagram of the DFIG in the synchronous rotating frame (SRF) is presented in Fig. 2. By employing the motor convention, the voltage and flux linkage equations of the DFIG can be given as:

$$\begin{cases} U_{sdq} = R_s I_{sdq} + \frac{d}{dt} \psi_{sdq} + j\omega_1 \psi_{sdq} \\ U_{rdq} = R_r I_{rdq} + \frac{d}{dt} \psi_{rdq} + j\omega_{slip} \psi_{rdq} \end{cases} \quad (1)$$

$$\begin{cases} \psi_{sdq} = L_s I_{sdq} + L_m I_{rdq} \\ \psi_{rdq} = L_m I_{sdq} + L_r I_{rdq} \end{cases} \quad (2)$$

$$\begin{cases} \psi_{mdq} = L_m I_{sdq} + L_m I_{rdq} \\ L_s = L_m + L_{sr} \\ L_r = L_m + L_{rr} \end{cases} \quad (3)$$

where U , I , and ψ are the voltage, current, and flux linkage vectors, respectively; the subscripts s , r , and m represent the stator, rotor, and air-gap components, respectively; the subscripts d and q represent the d - and q -axis components, respectively; R and L are the resistance and inductance, respectively; L_{sr} and L_{rr} are the stator and rotor leakage inductance, respectively; t is the time; and ω_1 and ω_{slip} are the synchronous and slip angular frequencies, respectively.

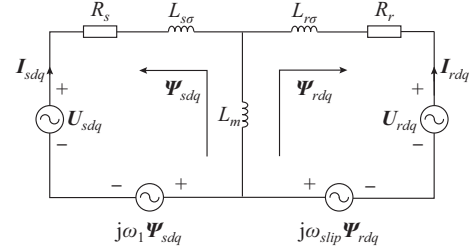


Fig. 2. Equivalent circuit diagram of DFIG in SRF.

Considering that the DFIG adopts a grid-forming control strategy, it can be equivalently modeled as a voltage source. The equivalent model of the DFIG connected to the PCC is shown in Fig. 3. Hence, the power transmitted from the DFIG to the PCC can be derived as:

$$\begin{cases} P_{DFIG} = \frac{U_{DFIG} U_{PCC}}{X_L} \sin(\theta_{DFIG} - \theta_{PCC}) \\ Q_{DFIG} = \frac{U_{DFIG} (U_{DFIG} - U_{PCC} \cos(\theta_{DFIG} - \theta_{PCC}))}{X_L} \end{cases} \quad (4)$$

where U_{DFIG} and θ_{DFIG} are the voltage amplitude and angle of the equivalent voltage source, respectively; U_{PCC} and θ_{PCC} are the voltage amplitude and angle at the PCC, respectively; X_L is the equivalent reactance from the DFIG to the PCC; and P_{DFIG} and Q_{DFIG} are the active power and reactive power transmitted from the DFIG to the PCC, respectively.

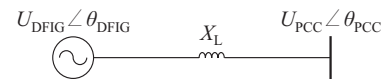


Fig. 3. Equivalent model of DFIG connected to PCC.

Due to the inductive characteristic of X_L , P_{DFIG} primarily depends on angle difference $\theta_{DFIG} - \theta_{PCC}$, while Q_{DFIG} mainly depends on U_{DFIG} .

B. Mathematical Model of DRU

According to the structure of DRU in Fig. 4, taking a 12-pulse diode rectifier as an example, the DC voltage of DRU V_{Rdc} can be obtained as [35]:

$$V_{Rdc} = \sqrt{U_{Rd}^2 + U_{Rq}^2} - R_\mu I_{Rdc} \quad (5)$$

where U_{Rd} and U_{Rq} are the d - and q -axis components of AC voltage of DRU, respectively; I_{Rdc} is the DC current of DRU; and R_μ is the equivalent commutation resistance, which can be calculated as:

$$R_\mu = 3\omega_1 L_{RT} / \pi \quad (6)$$

where L_{RT} is the leakage inductance of the DRU transformer.

In addition, the DC current of DRU I_{Rdc} can be derived as:

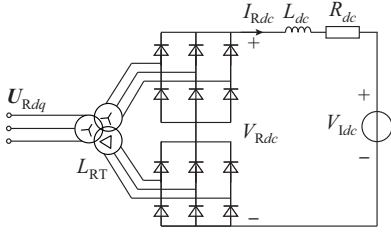


Fig. 4. Structure of DRU.

$$V_{Rdc} - V_{ldc} = R_{dc} I_{Rdc} \quad (7)$$

where R_{dc} is the resistance of DC cable; and V_{ldc} is the DC voltage of MMC.

Based on (5) and (7), the active and reactive power of DRU can be obtained as [20]:

$$\begin{cases} P_R = V_{Rdc} I_{Rdc} = \\ \frac{1}{(R_{dc} + R_\mu)^2} \left(R_{dc} \sqrt{U_{Rd}^2 + U_{Rq}^2} + R_\mu V_{ldc} \right) \left(\sqrt{U_{Rd}^2 + U_{Rq}^2} - V_{ldc} \right) \\ Q_R = \frac{2\mu - \sin 2\mu}{1 - \cos 2\mu} P_R \end{cases} \quad (8)$$

where P_R and Q_R are the active and reactive power of DRU, respectively; and μ is the DRU commutation angle, which can be calculated as:

$$\mu = \arccos \left(1 - 2R_\mu I_{Rdc} / \sqrt{U_{Rd}^2 + U_{Rq}^2} \right) \quad (9)$$

The AC voltage of DRU U_{Rdq} can be considered equivalent to the voltage of the PCC. Therefore, the active power transmitted by the DRU depends on the voltage magnitude of the PCC, while reactive power increases nonlinearly with the active power.

C. Self-synchronization Mechanism

For grid-forming devices connected to a conventional power grid, self-synchronization is achieved through P - f and Q - V control loops. This is because the imbalance of active power caused by load switching leads to frequency deviations. However, as shown in (8), the active power transmitted by the DRU depends on the voltage magnitude. Therefore, the self-synchronization mechanism of grid-forming devices connected to DRU-HVDC system differs significantly from that in conventional power grids.

Since the self-synchronization mechanism primarily focuses on the power balance between the DFIG and the DRU, the following power flow analysis is based on a quasi-static network model. In addition, to simplify the analysis, the dynamics of the inner control loop is ignored in this subsection due to its small time scale.

Based on the power characteristics of the DFIG and the DRU, P - V and Q - f control loops [24] can be designed to achieve self-synchronized operation of the DFIG in offshore wind farm connected to DRU-HVDC system. The self-synchronization mechanism of the offshore wind farm is illustrated in Fig. 5. If the active power reference of DFIG1 increases, its frequency is incrementally adjusted through the P - V control loop and the Q - f control loop based on the reactive power characteristics of the DFIG. This adjustment allows the active power reference to be tracked through the ac-

tive power characteristics of the DFIG. Additionally, the increase in the active power of DFIG1 causes the active power transmitted by the DRU to rise. The power characteristics of the DRU lead to an increase in the reactive power of the DRU. According to the reactive power sharing strategy in [27], the reactive power of the remaining DFIGs may also increase. Through the Q - f control loop, the frequencies of the remaining DFIGs may rise accordingly, achieving synchronization of the offshore wind farm.

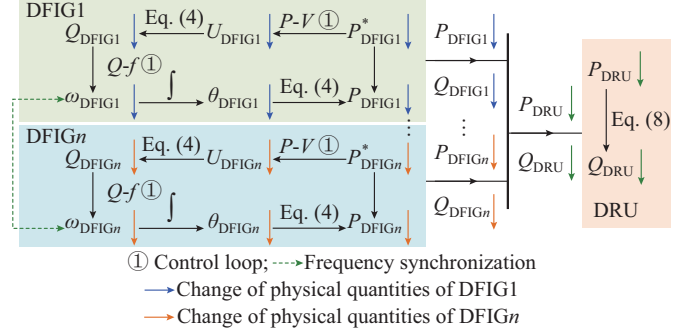


Fig. 5. Self-synchronization mechanism of offshore wind farm.

III. PROPOSED STRATEGY

It should be noted that the power of the DFIG is primarily delivered through the stator. Therefore, the RSC adopts the grid-forming control strategy, while the GSC employs the traditional control strategy.

On the basis of the self-synchronization mechanism, the self-synchronized grid-forming control strategy for DFIG in offshore wind farm connected to DRU-HVDC system is proposed in this section.

A. Active Power and Amplitude of Air-gap Flux Linkage Control Loop

The P - V control loop is firstly designed, which specifically refers to the active power and amplitude of air-gap flux linkage control loop. A PI controller is selected to track the reference of the active power, and its output is set as the amplitude reference of the air-gap flux linkage. The corresponding expression of the control structure can be written as:

$$|\psi_m^*| = \left(k_{pp} + \frac{k_{pi}}{s} \right) (P_s^* - P_s) \quad (10)$$

where $|\psi_m^*|$ and P_s^* are the amplitude reference of the air-gap flux linkage and the reference of the active power output by the stator of the DFIG, respectively; k_{pp} and k_{pi} are the proportional and integral parameters of the PI controller, respectively; and P_s is the active power output by the stator of the DFIG.

To maximize wind energy utilization under varying wind speeds, P_s^* is typically determined by the maximum power point tracking (MPPT) [36], which can be derived as:

$$P_s^* = \frac{P_m}{1 - sl} - P_{cus} = \frac{0.5\rho\pi R^2 v^3 C_p(\lambda, \beta)}{1 - sl} - P_{cus} \quad (11)$$

where P_m is the total input mechanical power; ρ is the air density; R is the blade radius; v is the wind speed; $C_p(\lambda, \beta)$ is the wind energy utilization coefficient; λ and β are the tip

The GSC employs a cascaded control structure with an outer control loop for DC-link voltage and an inner control loop for current, regulating the DC-link voltage of the DFIG. The RSC utilizes the proposed strategy to achieve self-synchronization of the DFIG in offshore wind farm connected to DRU-HVDC system. Since the primary characteristics of the DFIG are determined by the RSC, the GSC is neglected in the subsequent analysis.

In Fig. 6, \mathbf{U}_{gabc} and \mathbf{U}_{gdq} are the abc -axis and dq -axis components of the GSC voltage, respectively; \mathbf{I}_{gabc} and \mathbf{I}_{gdq} are the abc -axis and dq -axis components of the GSC current, respectively; k_{PLLp} and k_{PLLi} are the proportional and integral parameters of the PI-based PLL controller, respectively; k_{Vdcp} and k_{Vdci} are the proportional and integral parameters of the PI-based DC-link voltage controller, respectively; k_{Igp} and k_{Igi} are the proportional and integral parameters of the PI-based GSC current controller, respectively; V_{dc}^* and V_{dc} are the reference and actual values of the DC-link voltage, respectively; I_{gd}^* and I_{gq}^* are the d - and q -axis reference values of the GSC current, respectively; U_{id}^* and U_{iq}^* are the d - and q -axis reference values of the GSC control voltage, respectively; ω_g and θ_g are the angular frequency and degree of the GSC voltage, respectively; ω_r and θ_r are the angular frequency and degree of the DFIG rotor, respectively; R_g and L_g are the resistance and inductance of the GSC filter, respectively; \mathbf{U}_{sabc} , \mathbf{I}_{sabc} , and \mathbf{I}_{rabc} are the abc -axis components of the DFIG stator voltage, DFIG stator current, and DFIG rotor current, respectively; and S_{RSC} and S_{GSC} are the RSC and GSC switching signals, respectively.

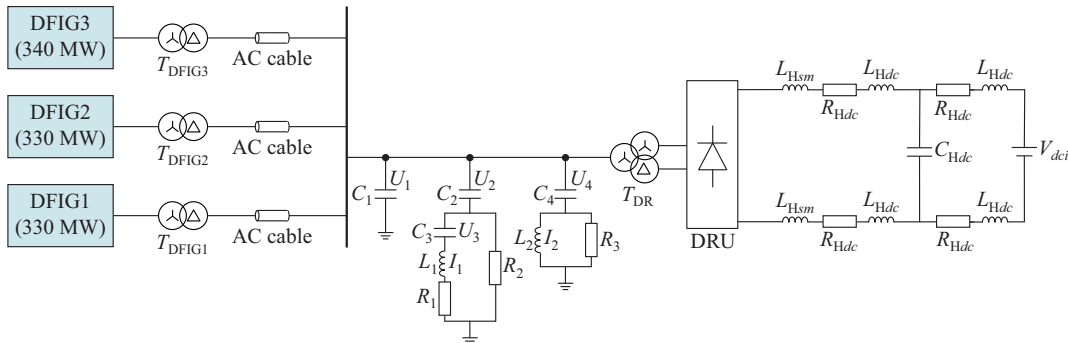


Fig. 7. Structure of 1000 MW DFIG in offshore wind farm connected to DRU-HVDC system.

B. State Space Model of DFIG

By combining (SA1)-(SA9) in Supplementary Material A, the state space model of the DFIG $_i$ is given as:

$$\begin{cases} \frac{d\Delta\mathbf{x}_{DFIGi}}{dt} = \mathbf{A}_{DFIGi}\Delta\mathbf{x}_{DFIGi} + \mathbf{B}_{DFIGi}\Delta\mathbf{u}_{DFIGi} \\ \Delta\mathbf{y}_{DFIGi} = \mathbf{C}_{DFIGi}\Delta\mathbf{x}_{DFIGi} \end{cases} \quad (18)$$

where Δ denotes the small-signal quantity; the subscript i denotes the i^{th} DFIG; $\Delta\mathbf{x}_{DFIGi} = [\Delta\omega_{li}^*, \Delta\delta_i, \Delta x_{pi}, \Delta x_{rldi}, \Delta x_{lrqi}, \Delta I_{rdi}, \Delta I_{rqi}, \Delta I_{sdi}, \Delta I_{sqi}]^T$; $\Delta\mathbf{u}_{DFIGi} = [\Delta U_{sdi}, \Delta U_{sqi}, \Delta\omega_{com}]^T$, ω_{com} is the angular velocity of the common rotating reference frame; δ is the angle difference between the VSRF of the DFIG and the common rotating reference frame; x_{rldi} and x_{lrqi} are the state variables of d - and q -axis rotor current controller, re-

D. Discussion of Fault Ride-through Control

The operation of PMSG in offshore wind farm connected to DRU-HVDC system under fault condition is extensively studied in [22], considering the onshore and offshore AC grid faults, DC cable faults, and internal DRU faults. The corresponding methods in [22] can be applied to the DFIG in offshore wind farm connected to DRU-HVDC system. However, unlike PMSG, DFIG requires additional consideration of transient flux components during fault ride-through. Interestingly, the proposed strategy in this paper adopts the air-gap flux linkage as a virtual internal electromotive force, enabling effective control of transient flux components through a rotor current-based inner flux loop [37]. Furthermore, the attenuation of the transient flux component can be further accelerated by incorporating the feedforward based on the derivative of the current reference [38] or the compensation of the rotor voltage [39].

IV. STABILITY ANALYSIS

A. Study Case

To verify the stability of the proposed strategy, the state-space model of a 1000 MW DFIG in offshore wind farm connected to the DRU-HVDC system is built, with its structure illustrated in Fig. 7. The offshore wind farm consists of three aggregated DFIGs with capacities of 330, 330, and 340 MW, respectively, whose parameters are shown in Supplementary Material A Table SAI. Besides, the parameters of the offshore AC system and DRU-HVDC system are listed in Supplementary Material A Table SAII.

spectively; x_{pi} is the state variable of P - V controller; $\Delta\mathbf{y}_{DFIGi} = [\Delta\omega_{li}^*, \Delta I_{sdi}, \Delta I_{sqi}]^T$ is the output vector of the DFIG state-space model; and \mathbf{A}_{DFIGi} and \mathbf{B}_{DFIGi} are the state and input matrices of the state-space model of DFIG, respectively.

Each DFIG is modeled in its own dq reference frame, with the rotational frequency determined by its power controller. To integrate all DFIGs into one reference frame, the reference frame of one DFIG is designated as the common DQ reference frame, and the output variables of the remaining DFIGs are transformed into common reference frame. The coordinate transformation expression can be derived as:

$$\begin{bmatrix} \Delta I_{sDi} \\ \Delta I_{sQi} \end{bmatrix} = \begin{bmatrix} \cos \delta_{i0} & -\sin \delta_{i0} \\ \sin \delta_{i0} & \cos \delta_{i0} \end{bmatrix} \begin{bmatrix} \Delta I_{sdi} \\ \Delta I_{sqi} \end{bmatrix} + \begin{bmatrix} -I_{sdi0} \sin \delta_{i0} - I_{sqi0} \cos \delta_{i0} \\ I_{sdi0} \cos \delta_{i0} - I_{sqi0} \sin \delta_{i0} \end{bmatrix} \begin{bmatrix} \Delta \delta_i \end{bmatrix} \quad (19)$$

$$\begin{bmatrix} \Delta U_{sdi} \\ \Delta U_{sqi} \end{bmatrix} = \begin{bmatrix} \cos \delta_{i0} & \sin \delta_{i0} \\ -\sin \delta_{i0} & \cos \delta_{i0} \end{bmatrix} \begin{bmatrix} \Delta U_{sDi} \\ \Delta U_{sQi} \end{bmatrix} + \begin{bmatrix} -U_{sD0} \sin \delta_{i0} + U_{sQ0} \cos \delta_{i0} \\ -U_{sD0} \cos \delta_{i0} - U_{sQ0} \sin \delta_{i0} \end{bmatrix} [\Delta \delta_i] \quad (20)$$

where subscripts D and Q denote the d - and q -axis components of the common DQ reference frame, respectively; and the subscript 0 denotes the steady-state quantity. The reference frame of DFIG1 is chosen as the common DQ reference frame in the following analysis.

C. State-space Model of Offshore AC System

The state-space model of the offshore AC system, which includes the i^{th} DFIG transformer $T_{\text{DFIG}i}$, AC cable, and reactive power compensation device, has been established in [15] and is rewritten as:

$$\begin{cases} \frac{d\Delta \mathbf{x}_{AC}}{dt} = \mathbf{A}_{AC} \Delta \mathbf{x}_{AC} + \mathbf{B}_{AC} \Delta \mathbf{u}_{AC} \\ \Delta \mathbf{y}_{AC} = \mathbf{C}_{AC} \Delta \mathbf{x}_{AC} \end{cases} \quad (21)$$

where $\Delta \mathbf{x}_{AC} = [\Delta U_{sD1}, \Delta U_{sQ1}, \Delta I_{\text{WT}D1}, \Delta I_{\text{WT}Q1}, \Delta U_{\text{AC}1D1}, \Delta U_{\text{AC}1Q1}, \Delta I_{\text{AC}1D1}, \Delta I_{\text{AC}1Q1}, \Delta U_{sD2}, \Delta U_{sQ2}, \Delta I_{\text{WT}D2}, \Delta I_{\text{WT}Q2}, \Delta U_{\text{AC}1D2}, \Delta U_{\text{AC}1Q2}, \Delta I_{\text{AC}2D1}, \Delta I_{\text{AC}2Q1}, \Delta U_{sD3}, \Delta U_{sQ3}, \Delta I_{\text{WT}D3}, \Delta I_{\text{WT}Q3}, \Delta U_{\text{AC}1D3}, \Delta U_{\text{AC}1Q3}, \Delta I_{\text{AC}3D1}, \Delta I_{\text{AC}3Q1}, \Delta U_{\text{ACD}}, \Delta U_{\text{ACQ}}, \Delta U_{\text{F}2D}, \Delta U_{\text{F}2Q}, \Delta U_{\text{F}3D}, \Delta U_{\text{F}3Q}, \Delta U_{\text{F}4D}, \Delta U_{\text{F}4Q}, \Delta I_{\text{F}1D}, \Delta I_{\text{F}1Q}, \Delta I_{\text{F}2D}, \Delta I_{\text{F}2Q}]^T$; I_{WT} is the current of the inductance of DFIG transformer; $U_{\text{AC}1}$ is the voltage of the equivalent capacitance of the AC cable; I_{AC} is the current of the equivalent inductance of the AC cable; U_{AC} is the voltage of the capacitance C_1 ; $U_{\text{F}2}$, $U_{\text{F}3}$, and $U_{\text{F}4}$ are the voltages of the filter capacitances C_2 , C_3 , and C_4 , respectively; $I_{\text{F}1}$ and $I_{\text{F}2}$ are the currents of the filter inductances L_1 and L_2 , respectively; $\Delta \mathbf{u}_{AC} = [\Delta I_{sD1}, \Delta I_{sQ1}, \Delta U_{\text{AC}1D1}, \Delta U_{\text{AC}1Q1}, \Delta I_{sD2}, \Delta I_{sQ2}, \Delta U_{\text{AC}2D1}, \Delta U_{\text{AC}2Q1}, \Delta I_{sD3}, \Delta I_{sQ3}, \Delta U_{\text{AC}3D1}, \Delta U_{\text{AC}3Q1}, \Delta \omega_{\text{com}}, \Delta I_{\text{RD}}, \Delta I_{\text{RQ}}, \Delta I_{\text{ACD}}, \Delta I_{\text{ACQ}}]^T$; I_{R} is the AC current of DRU; and $\Delta \mathbf{y}_{AC} = [\Delta U_{sD1}, \Delta U_{sQ1}, \Delta U_{sQ3}, \Delta I_{\text{AC}3D1}, \Delta I_{\text{AC}3Q1}, \Delta U_{\text{ACD}}, \Delta U_{\text{ACQ}}]^T$.

D. State-space Model of DRU

The state-space model of DRU system, which includes the DRU, transformer T_{DR} , DC cable, and DC smoothing reactance, has been established in [24] and is rewritten as:

$$[\Delta I_{\text{RD}}, \Delta I_{\text{RQ}}, \Delta V_{\text{Rdc}}]^T = \mathbf{A}_{\text{DRU}} [\Delta \omega_{\text{com}}, \Delta U_{\text{RD}}, \Delta U_{\text{RQ}}, \Delta I_{\text{Rdc}}]^T \quad (22)$$

$$\begin{cases} \frac{d\Delta \mathbf{x}_{DC}}{dt} = \mathbf{A}_{DC} \Delta \mathbf{x}_{DC} + \mathbf{B}_{DC} \Delta \mathbf{u}_{DC} \\ \Delta \mathbf{y}_{DC} = \mathbf{C}_{DC} \Delta \mathbf{x}_{DC} \end{cases} \quad (23)$$

where $\Delta \mathbf{x}_{DC} = [\Delta I_{\text{Rdc}}, \Delta I_{\text{Idc}}, \Delta V_{\text{Hdc}}]^T$; I_{Idc} is the DC current on the MMC side; $\Delta \mathbf{u}_{DC} = [\Delta V_{\text{Rdc}}]$; $\Delta \mathbf{y}_{DC} = [\Delta U_{\text{RD}}, \Delta U_{\text{RQ}}]^T$; \mathbf{A}_{DRU} is the small-signal model matrix of the DRU; and \mathbf{A}_{DC} , \mathbf{B}_{DC} , and \mathbf{C}_{DC} are the state, input, and output matrices of the state-space model of the DRU, respectively.

E. State-space Model of Whole System

By combining (18) - (23), the state space model of the whole system is given as:

$$\begin{cases} \frac{d\Delta \mathbf{x}_{\text{sys}}}{dt} = \mathbf{A}_{\text{sys}} \Delta \mathbf{x}_{\text{sys}} + \mathbf{B}_{\text{sys}} \Delta \mathbf{u}_{\text{sys}} \\ \Delta \mathbf{y}_{\text{sys}} = \mathbf{C}_{\text{sys}} \Delta \mathbf{x}_{\text{sys}} \end{cases} \quad (24)$$

where $\Delta \mathbf{x}_{\text{sys}} = [\Delta \mathbf{x}_{\text{DFIG}1}, \Delta \mathbf{x}_{\text{DFIG}2}, \Delta \mathbf{x}_{\text{DFIG}3}, \Delta \mathbf{x}_{\text{AC}}, \Delta \mathbf{x}_{\text{DC}}]^T$; $\Delta \mathbf{u}_{\text{sys}} = [\Delta \mathbf{u}_{\text{DFIG}1}, \Delta \mathbf{u}_{\text{DFIG}2}, \Delta \mathbf{u}_{\text{DFIG}3}, \Delta \mathbf{u}_{\text{AC}}, \Delta \mathbf{u}_{\text{DC}}]^T$; $\Delta \mathbf{y}_{\text{sys}} = [\Delta \mathbf{y}_{\text{DFIG}1}, \Delta \mathbf{y}_{\text{DFIG}2}, \Delta \mathbf{y}_{\text{DFIG}3}, \Delta \mathbf{y}_{\text{AC}}, \Delta \mathbf{y}_{\text{DC}}]^T$; and \mathbf{A}_{sys} , \mathbf{B}_{sys} , and \mathbf{C}_{sys} are the state, input, and output matrices of the state-space model of the whole system, respectively.

F. Stability Analysis

By substituting the system parameters listed in Supplementary Material A Tables SAI and SAII into \mathbf{A}_{sys} , the eigenvalues of the rated operating condition are calculated, as presented in Table II, where λ_m represents the m^{th} eigenvalue, and $\lambda_{m,n}$ represents the conjugate eigenvalue. It can be seen that the real parts of all eigenvalues are negative, which means the investigated system working under the rated operating condition is proven to be stable. Moreover, the dominant states of these conditions indicate that the control parameters of the DFIG dominate the system behavior.

TABLE II
EIGENVALUES OF RATED OPERATING CONDITION

Eigenvalue	Dominant state	Eigenvalue	Dominant state
$\lambda_1 = -9962.5$	$\Delta \omega_{11}^*$	$\lambda_2 = -9962.5$	$\Delta \omega_{13}^*$
$\lambda_{3,4} = -0.44 \pm j113.39$	$\Delta U_{\text{AC}1D3}$	$\lambda_{5,6} = -0.44 \pm j113.39$	$\Delta U_{\text{AC}1D1}$
$\lambda_{7,8} = -0.28 \pm j111.44$	$\Delta U_{\text{AC}1Q3}$	$\lambda_{9,10} = -0.28 \pm j111.44$	$\Delta U_{\text{AC}1Q1}$
$\lambda_{11,12} = -0.41 \pm j87.58$	$\Delta U_{\text{AC}1D2}$	$\lambda_{13,14} = -0.41 \pm j85.65$	$\Delta U_{\text{AC}1Q3}$
$\lambda_{15,16} = -9.42 \pm j61.23$	ΔU_{sD2}	$\lambda_{17,18} = -10.92 \pm j55.48$	ΔU_{sD3}
$\lambda_{19,20} = -10.92 \pm j55.48$	ΔU_{sD1}	$\lambda_{21,22} = -0.07 \pm j30.76$	ΔU_{sQ2}
$\lambda_{23,24} = -28.03 \pm j8.46$	ΔU_{sD1}	$\lambda_{25,26} = -28.03 \pm j8.46$	ΔU_{sD3}
$\lambda_{27,28} = -26.47 \pm j7.24$	ΔU_{sD2}	$\lambda_{29,30} = -0.24 \pm j20.24$	ΔU_{sQ1}
$\lambda_{31,32} = -0.24 \pm j20.24$	ΔU_{sQ3}	$\lambda_{33,34} = -5.07 \pm j11.97$	ΔI_{2Q}
$\lambda_{35,36} = -5.06 \pm j10.06$	ΔI_{2D}	$\lambda_{37,38} = -10.04 \pm j3.69$	$\Delta U_{sD1}, \Delta U_{sD3}$
$\lambda_{39,40} = -1.92 \pm j7.5$	Δx_{P1}	$\lambda_{41,42} = -1.92 \pm j7.51$	Δx_{P3}
$\lambda_{43,44} = -2.56 \pm j6.29$	Δx_{P2}	$\lambda_{45,46} = -6.8 \pm j0.92$	$\Delta I_{1D}, \Delta I_{1Q}$
$\lambda_{47,48} = -0.06 \pm j1.91$	$\Delta x_{\text{Ird}1}$	$\lambda_{49,50} = -0.15 \pm j0.97$	ΔU_{3Q}
$\lambda_{51,52} = -0.85 \pm j0.42$	$\Delta x_{\text{Ird}3}$	$\lambda_{53,54} = -1.73 \pm j0.47$	$\Delta x_{\text{Ird}1}$
$\lambda_{55,56} = -1.76 \pm j0.45$	$\Delta x_{\text{Ird}2}$	$\lambda_{57,58} = -1.72 \pm j0.46$	$\Delta x_{\text{Ird}3}$
$\lambda_{59} = -39.59$	ΔI_{2D}	$\lambda_{60} = -33.33$	ΔI_{2Q}
$\lambda_{61} = -14.7$	ΔU_{sD2}	$\lambda_{62} = -3.21$	ΔI_{Rdc}
$\lambda_{63} = -0.42$	Δx_{P1}	$\lambda_{64} = -0.45$	$\Delta x_{\text{Ird}2}$
$\lambda_{65} = -0.45$	$\Delta x_{\text{Ird}1}$	$\lambda_{66} = -9962.5$	$\Delta \omega_{12}^*$

To further analyze the system stability, the root locus of the most-affected poles under different conditions are shown in Fig. 8. Figure 8(a) presents the root locus with output power (wind speed) of DFIGs, demonstrating that the whole system remains stable with output power increasing from 0.1 p. u. to 1.0 p. u.. Besides, the electrical distance among DFIGs has an impact on the system stability. In this paper, the impedances of the AC cables and transformers among DFIGs are used to represent the electrical distances. The actual impedance values, provided in Supplementary Material A Table SAII, are used as the base per-unit calculation. As the electrical distance decreases, the system gradually becomes unstable, as illustrated in Fig. 8(b). Moreover, as shown in Fig. 8(c) and (d), the system stability also deteriorates.

rates with the increases of k_{Irdp} and k_{Pp} .

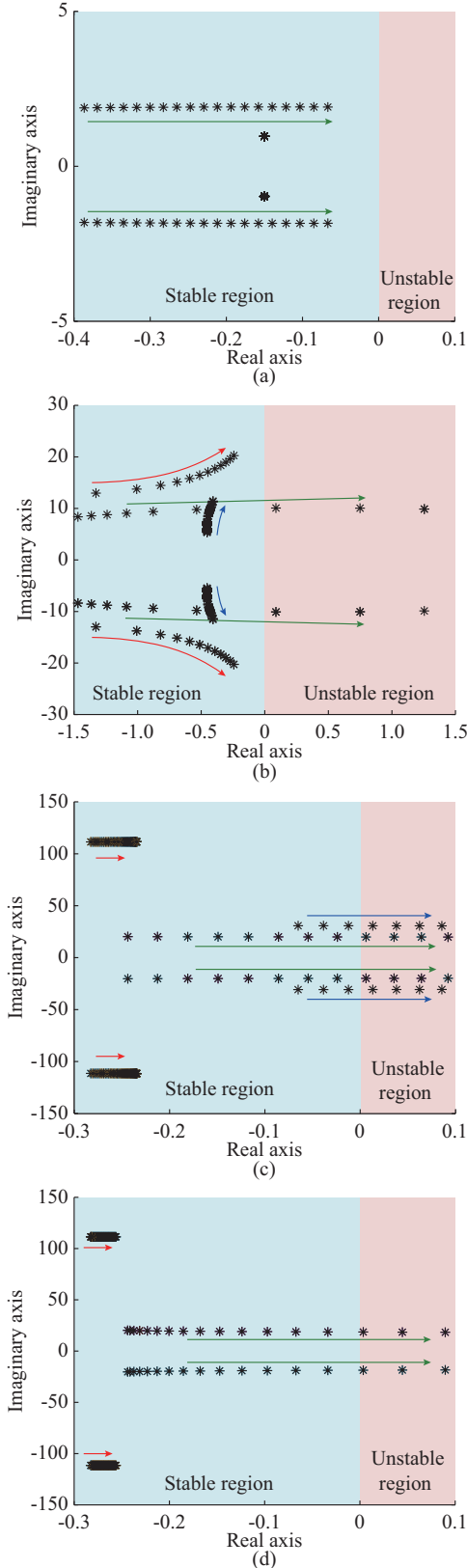


Fig. 8. Root locus of most-affected poles under different conditions. (a) Output power (wind speed) of DFIGs increasing from 0.1 p.u. to 1.0 p.u.. (b) Electrical distance among DFIGs decreasing from 1.0 p.u. to 0.1 p.u.. (c) k_{Irdp} of DFIGs increasing from 5 to 15. (d) k_{Pp} of DFIGs increasing from 0.1 to 5.0.

V. ELECTROMAGNETIC OSCILLATION REDUCTION METHOD

Due to the natural commutation characteristics of the DRU, a 12-pulse DRU, for example, generates the significant 11th- and 13th-order harmonic currents on the AC side. This leads to noticeable oscillations in power and torque, which can affect the stable operation of the DFIG. Additionally, torque oscillations can shorten the lifespan of the DFIG shaft system. Hence, an electromagnetic oscillation reduction method is proposed in this section.

A. Mathematical Model of Electromagnetic Oscillation

Assuming that the offshore grid voltage contains the fundamental frequency component as well as the 11th- and 13th-order harmonics, the components of the stator and rotor sides of the DFIG in the VSRF can be expressed as:

$$\begin{cases} \mathbf{F}_{sdq}^+ = \mathbf{F}_{sdq+}^+ + \mathbf{F}_{sdq11-}^{11-} e^{-j12\omega_1 t} + \mathbf{F}_{sdq13+}^{13+} e^{j12\omega_1 t} \\ \mathbf{F}_{rdq}^+ = \mathbf{F}_{rdq+}^+ + \mathbf{F}_{rdq11-}^{11-} e^{-j12\omega_1 t} + \mathbf{F}_{rdq13+}^{13+} e^{j12\omega_1 t} \end{cases} \quad (25)$$

where \mathbf{F} represents the vector of physical quantities; the superscripts +, 11-, and 13+ represent the rotating reference frames for the positive fundamental, negative 11th-order, and positive 13th-order, respectively; and the subscripts +, 11-, and 13+ represent the positive fundamental, negative 11th-order, and positive 13th-order components, respectively.

Based on (1)-(3) and (25), the expressions for the DFIG stator current and flux linkage can be derived as:

$$\begin{cases} \mathbf{I}_{sdq}^+ = \frac{\Psi_{mdq}^+}{L_m} - \mathbf{I}_{rdq}^+ \\ \Psi_{sdq}^+ = L_s \frac{\Psi_{mdq}^+}{L_m} - L_{s\sigma} \mathbf{I}_{rdq}^+ \end{cases} \quad (26)$$

With the stator resistance neglected, the DFIG stator voltage can be calculated as:

$$\mathbf{U}_{sdq}^+ \approx \frac{d}{dt} \Psi_{sdq}^+ + j\omega_1 \Psi_{sdq}^+ = j\omega_1 \left(L_s \frac{\Psi_{mdq}^+}{L_m} - L_{s\sigma} \mathbf{I}_{rdq}^+ \right) \quad (27)$$

According to (26) and (27), the instantaneous output active and reactive power of the stator can be calculated as:

$$\begin{cases} P_s = -1.5 \text{Re}(\mathbf{U}_{sdq}^+ \mathbf{I}_{sdq}^{+*}) = \\ P_{s,dc} + \sum_{i=12,24} P_{s,\cos(i)} \cos(i\omega_1 t) + \sum_{i=12,24} P_{s,\sin(i)} \sin(i\omega_1 t) \\ Q_s = -1.5 \text{Im}(\mathbf{U}_{sdq}^+ \mathbf{I}_{sdq}^{+*}) = \\ Q_{s,dc} + \sum_{i=12,24} Q_{s,\cos(i)} \cos(i\omega_1 t) + \sum_{i=12,24} Q_{s,\sin(i)} \sin(i\omega_1 t) \end{cases} \quad (28)$$

where the subscripts dc, cos, and sin represent the DC, cosine, and sine components, respectively. The expressions are shown in Supplementary Material A (SA10).

The electromagnetic power of the DFIG can be regarded as the sum of the active power generated by $j\omega_1 \Psi_{sdq}^+$ and $j\omega_{slip} \Psi_{rdq}^+$, which can be expressed in Supplementary Material A (SA11) as:

$$\begin{aligned} P_e &= -1.5 \text{Re}(j\omega_1 \Psi_{sdq}^+ \mathbf{I}_{sdq}^{+*} + j\omega_{slip} \Psi_{rdq}^+ \mathbf{I}_{rdq}^{+*}) = 1.5\omega_r \text{Im}(\mathbf{I}_{rdq}^+ \Psi_{mdq}^{+*}) = \\ &P_{e,dc} + \sum_{i=12,24} P_{e,\cos(i)} \cos(i\omega_1 t) + \sum_{i=12,24} P_{e,\sin(i)} \sin(i\omega_1 t) \end{aligned} \quad (29)$$

Furthermore, the electromagnetic torque can be obtained as:

$$T_e = \frac{pP_e}{\omega_r} \quad (30)$$

where p is the pole pair of the DFIG.

As represented in (28)-(30), both the instantaneous active power and reactive power of the stator and the electromagnetic torque contain the 12th-order and 24th-order harmonic components. It is worth noting that the 24th-order harmonic components are generated by the interaction between the 12th-order harmonic component of voltage/flux and the 12th-order harmonic of current. As the fast Fourier transform (FFT) result shows in Fig. 9, taking the electromagnetic torque as an example, the 24th-order harmonic component is relatively small compared with the DC component, which can be neglected. Hence, the following analysis focuses on the 12th-order harmonic component.

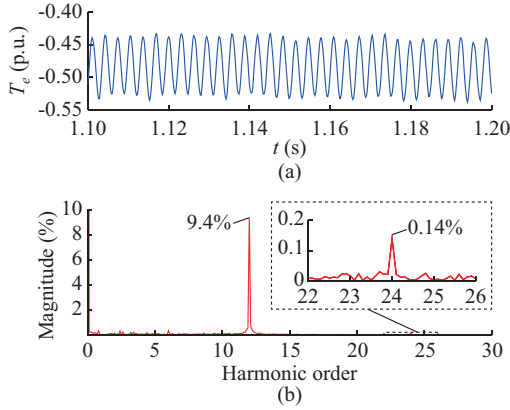


Fig. 9. Oscillation and FFT result of electromagnetic torque. (a) T_e . (b) FFT result.

B. Effect Law of dq -axis Current on Electromagnetic Oscillation

To clarify the correlations between the different electromagnetic oscillation components and the dq -axis components, the variance-based sensitivity analysis, i.e., Sobol indices [40], is adopted. Taking the dq -axis rotor currents of 12th-order as inputs, the 1st-order and total-effect indices of the sensitivity analysis are obtained based on the expressions of the electromagnetic oscillations. The results are shown in Figs. 10 and 11.

It can be seen in Fig. 10 that for the oscillation of active power, it is highly correlated with the q -axis rotor current, particularly the 13th-order component. Similarly, the oscillation of electromagnetic torque is also significantly correlated with the q -axis rotor current. In contrast, the oscillation of reactive power is more correlated with the d -axis rotor current. In addition, similar effect laws can be summarized according to the total-effect index in Fig. 11.

C. Illustration of Electromagnetic Oscillation Reduction Method

Since the primary oscillation component is 12th-order, the transfer function of the resonant controllers used in this paper can be set as:

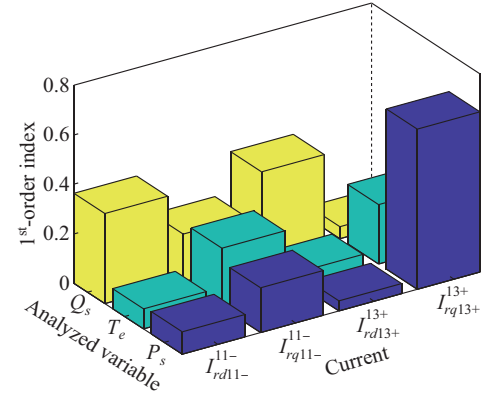


Fig. 10. 1st-order index of dq -axis rotor currents on electromagnetic oscillations.

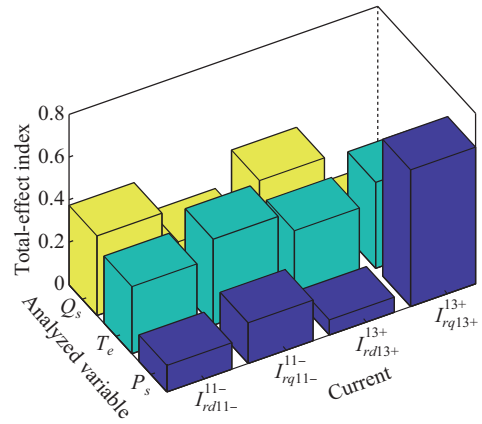


Fig. 11. Total-effect index of dq -axis rotor currents on electromagnetic oscillations.

$$G(s) = \frac{2k_{rs}\omega_c s}{s^2 + 2\omega_c s + (12\omega_1^*)^2} \quad (31)$$

where k_{rs} is the gain of the resonant controller; and ω_c is the bandwidth of the resonant controller, which is always designed within the range of 5-20 rad/s.

In addition, the resonant frequency of the resonant controller depends on the output of the Q - f control loop of the DFIG, enabling automatic tracking of the oscillation frequency.

The electromagnetic torque oscillations may reduce the fatigue strength and lifespan of mechanical components of the DFIG. Therefore, the electromagnetic torque oscillation control should be considered a priority. Based on the results of the sensitivity analysis, the direct torque resonant control loop should be designed on the q -axis.

Furthermore, reactive power oscillations are more closely related to the d -axis. Hence, direct reactive power resonant control can be designed on the d -axis, which does not conflict with the suppression of electromagnetic torque oscillations.

Consequently, the redesigned inner control loops considering electromagnetic oscillation reduction are shown in Fig. 12. To eliminate electromagnetic oscillations, the reference values of the resonant controllers are set to be zero.

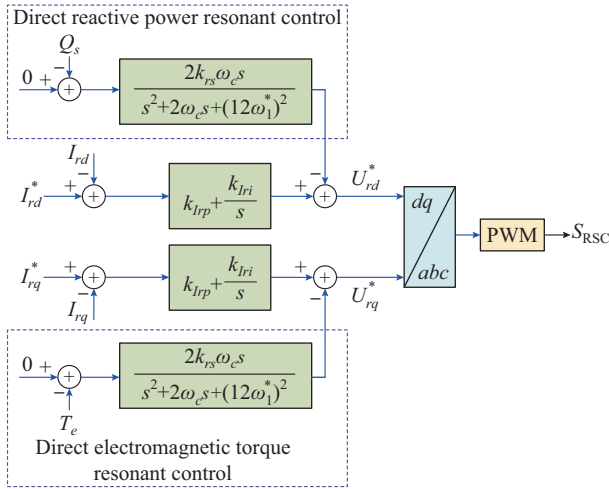


Fig. 12. Redesigned inner control loops considering electromagnetic oscillation reduction.

VI. SIMULATION VERIFICATIONS

To validate the effectiveness of the proposed strategy and the electromagnetic oscillation reduction method, the same system, which is studied in Section IV, is built in MATLAB/Simulink.

A. Performance of Start-up Process

The simulation results of the start-up process are shown in Fig. 13. At $t=0$ s, the DC-link voltage of the DFIG is controlled by the energy storage device to reach 1200 V. At $t=1.0$ s, the reference of the active power of DFIG1 is set to be 0.8 p.u..

It can be observed that the magnitude of the PCC voltage gradually increases with the reactive power generated by the reactive compensation device being absorbed by DFIG1. As the voltage continues to increase, the DRU conducts, beginning to transmit active power and consume reactive power. At $t=1.5$ s, DFIG1 successfully starts and tracks the reference of the active power.

At $t=2$ s, the reference of the active power of DFIG2 is set to be 0.4 p.u.. DFIG2 tracks the reference quickly and smoothly, without causing significant power fluctuations that may impact the stable operation of the offshore wind farm. As the active power transmitted by the DRU increases, the reactive power consumption also increases. In addition to the reactive power supplied by the reactive compensation device, both DFIG1 and DFIG2 generate equal reactive power, achieving reactive power sharing and enabling synchronized operation. After $t=3$ s, DFIG3 successfully starts and generates an active power of 0.6 p.u. as the reference. Besides, in the whole start-up process, the voltage and frequency of the offshore wind farm remain within acceptable ranges.

According to the simulation results, the proposed strategy enables the DFIG to form the AC grid of offshore wind farm connected to DRU-HVDC system, achieving self-synchronized operation of the DFIGs.

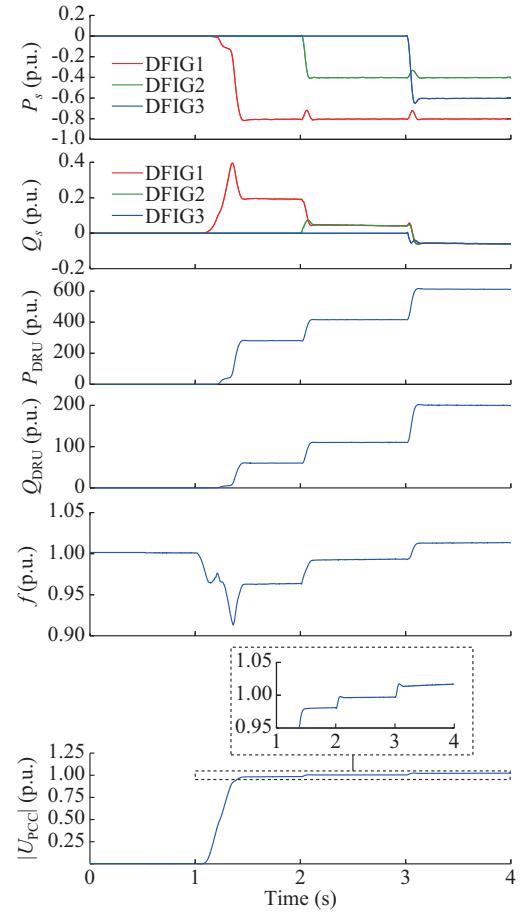


Fig. 13. Simulation results of start-up process.

B. Performance of Power Reference Change

Figure 14 presents the simulation results of power reference change. At $t=5$ s, the reference of the active power of DFIG1 gradually decreases from 0.8 p.u. to 0.2 p.u. at a rate of 2 p.u./s. As shown in Fig. 14(a), the output active power of DFIG1 gradually decreases to 0.2 p.u. and the output active power of other DFIGs is almost unaffected. During this process, the reactive power absorbed by the DRU decreases correspondingly. Due to the reactive power sharing control, the output reactive power of all DFIGs decreases uniformly, thereby achieving frequency unification across the offshore wind farm.

The performance of the offshore wind farm remains similar when the reference of the active power of DFIG changes. The simulation results demonstrate that the proposed strategy effectively ensures stable operation of the offshore wind farm during the variation of the output active power of DFIG.

C. Performance of Wind Speed Change

Figure 15 presents the simulation results of the wind speed change. When the wind speed decreases from 10 m/s to 8 m/s at 10 s, the mechanical input power of DFIG1 drops accordingly, leading to a reduction in its rotor speed. According to the MPPT, the active power reference of DFIG1 also decreases, and the system reaches a new equilibrium point.

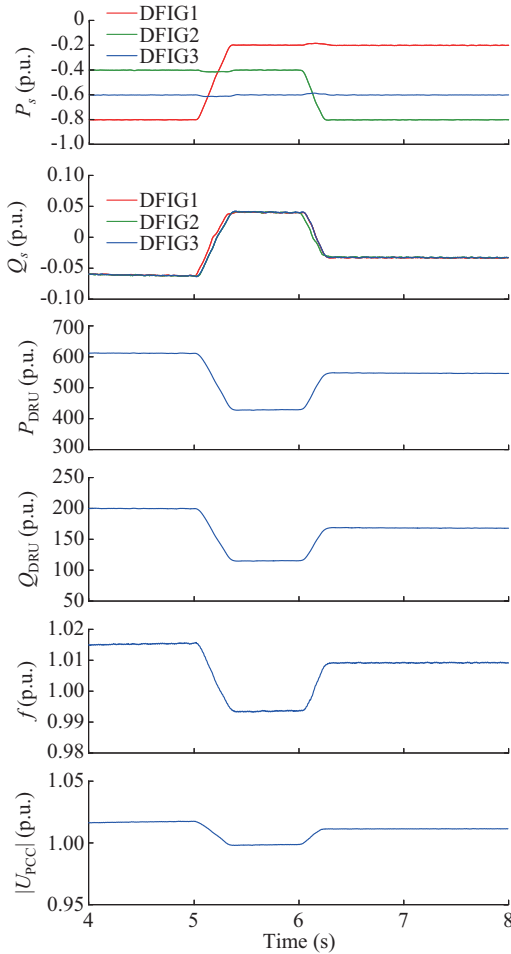


Fig. 14. Simulation results of power reference change.

It can be observed that DFIG1 operates effectively across both super-synchronous and sub-synchronous modes. Moreover, when the wind speed changes the reactive power remains evenly shared among the three DFIGs, maintaining synchronization of the system.

D. Performance of Electromagnetic Oscillation Reduction Method

It can be seen from Fig. 16 that during rapid changes of the operating point of offshore wind farm, taking a sudden increase in active power as an example, the passive compensation device fails to engage promptly, which leads to noticeable oscillations in the active and reactive power of DFIG. Besides, the electromagnetic torque contains a 12th-order oscillation, with the amplitude of the oscillation reaching 0.082 p.u..

Figure 17 exhibits the simulation results of the proposed electromagnetic oscillation reduction method. While the proposed method is enabled, the oscillations of both reactive power and electromagnetic torque are significantly suppressed. The FFT analysis of the electromagnetic torque reveals a reduction in its 12th-order component from 8.73% to 1.73%, with the total harmonic distortion (THD) decreasing from 8.89% to 3.69%.

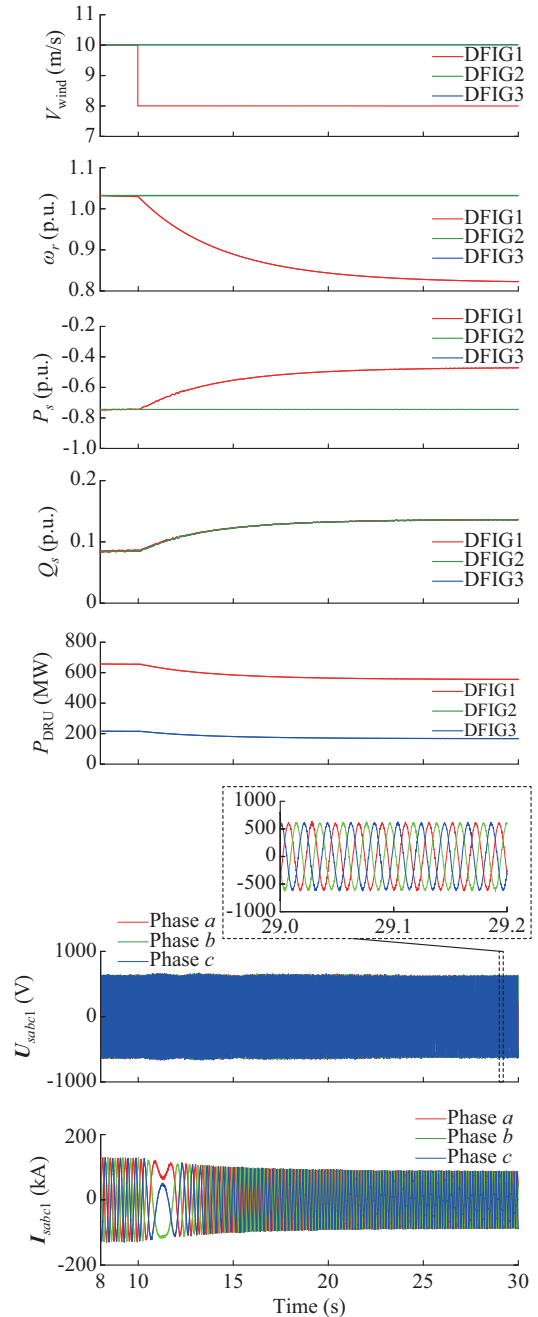


Fig. 15. Simulation results of wind speed change.

E. Verification of Stability Analysis

As shown in Supplementary Material A Fig. SA1(a), when the electrical distance is reduced to 0.1 p.u., DFIG1 operates stably.

At 2 s, DFIG2 starts up, leading to system instability, which is consistent with the theoretical analysis. Besides, at 3 s, k_{pp} and k_{irp} are increased, and the corresponding simulation results are shown in Supplementary Material A Fig. SA1(b) and (c), respectively. It can be seen that, as the control parameters increase, the system transits from a stable state to an unstable one, which aligns with the theoretical analysis results.

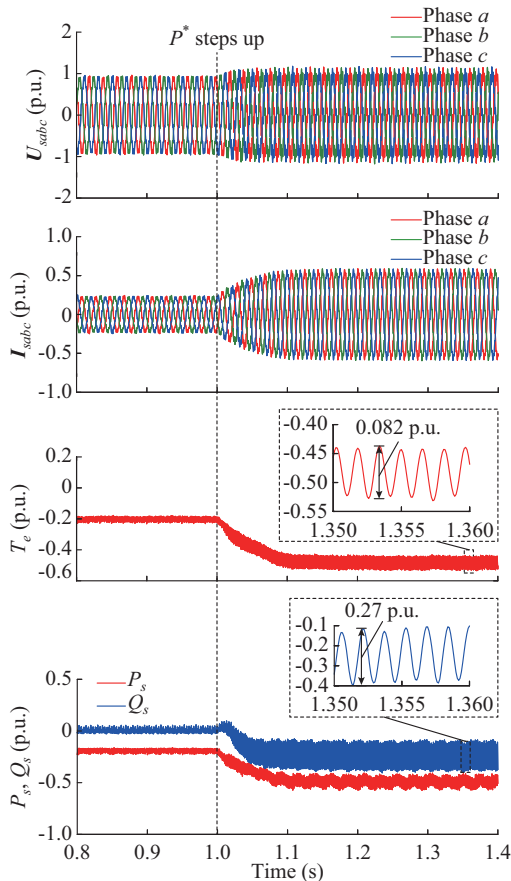


Fig. 16. Electromagnetic oscillations caused by DRU.

VII. CONCLUSION

To further reduce the cost on development of deep-sea wind power generation, this paper proposes a grid-forming control strategy for DFIG-based offshore wind farm connected to DRU-HVDC system. The simulation results demonstrate the effectiveness. The following conclusions can be summarized.

1) According to the unique voltage-power characteristic of the DRU, a novel self-synchronized control strategy for DFIG is put forward. With this strategy, the AC grid of the offshore wind farm connected to DRU can be established, and the frequency is regulated by all DFIGs.

2) The sensitivity analysis based on Sobol indices reveals the correlation between the dq -axis components of DFIG and electromagnetic oscillation components induced by DRU characteristic harmonics. It can be found that the q -axis components play important roles in the oscillations of the active power and electromagnetic torque, and the oscillation of the reactive power shows a stronger correlation with the d -axis components.

3) According to the results of the stability analysis, an electromagnetic oscillation reduction method based on the direct torque and power resonance control is designed. While the method is applied, the oscillations of the electromagnetic torque and the reactive power can be mitigated effectively.

The active and reactive power decoupling control method for DFIG-based offshore wind farm connected to DRU-HVDC system will be investigated in near future.

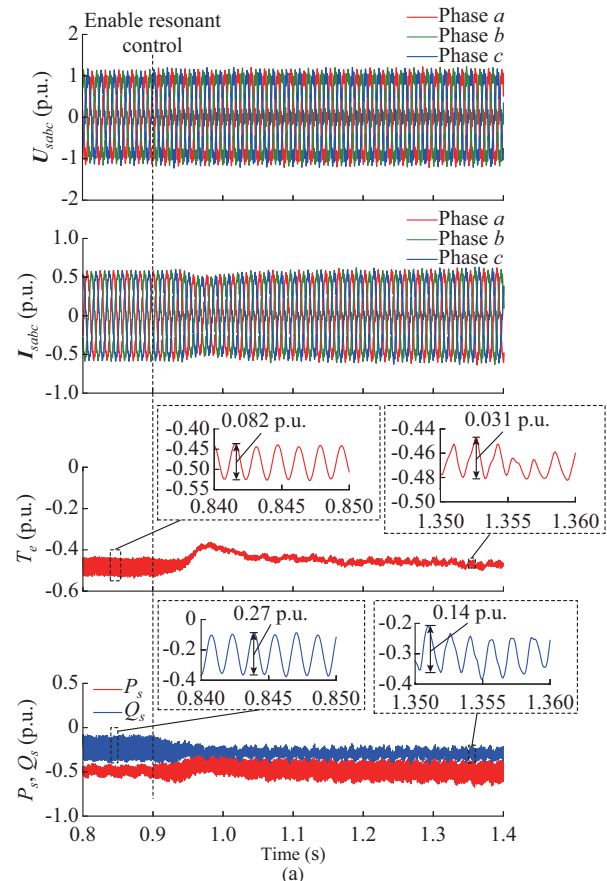


Fig. 17. Simulation results of proposed electromagnetic oscillation reduction method. (a) Waveforms. (b) FFT analysis of electromagnetic torque.

REFERENCES

- [1] GWEC. (2024, Dec.). Global offshore wind report 2024. [Online]. Available: <https://gwec.net/global-offshore-wind-report-2024/>
- [2] Y. Jin, Z. Zhang, and Z. Xu, "Proportion of grid-forming wind turbines in hybrid GFM-GFL offshore wind farms integrated with diode rectifier unit based HVDC system," *Journal of Modern Power Systems and Clean Energy*, vol. 13, no. 1, pp. 87-101, Jan. 2025.
- [3] C. Buchhagen, C. Rauscher, A. Menze *et al.*, "BorWin1 – first experiences with harmonic interactions in converter dominated grids," in *Proceedings of 2015 International ETG Congress*, Bonn, Germany, Nov. 2015, pp. 1-7.
- [4] J. Zhang and H. Wang, "Development of offshore wind power and foundation technology for offshore wind turbines in China," *Ocean Engineering*, vol. 266, p. 113256, Dec. 2022.
- [5] A. Nami, J. Liang, F. Dijkhuizen *et al.*, "Modular multilevel converters for HVDC applications: review on converter cells and functionalities," *IEEE Transactions on Power Electronics*, vol. 30, no. 1, pp. 18-36, Jan. 2015.
- [6] P. Sherman, X. Chen, and M. McElroy, "Offshore wind: an opportunity for cost-competitive decarbonization of China's energy economy," *Science Advances*, vol. 6, no. 8, p. eaax9571, Feb. 2020.

- [7] H. Xiao, H. Gan, Y. Dong *et al.*, "Control and capacity design of station-hybrid HVDC system with DRU and MMC in parallel for offshore wind power integration," *IEEE Transactions on Power Delivery*, vol. 39, no. 3, pp. 1783-1793, Jun. 2024.
- [8] R. Li and L. Xu, "A unidirectional hybrid HVDC transmission system based on diode rectifier and full-bridge MMC," *IEEE Journal of Emerging and Selected Topics in Power Electronics*, vol. 9, no. 6, pp. 6974-6984, Dec. 2021.
- [9] A. Nami, J. L. Rodríguez-Amenedo, S. Arnaltes *et al.*, "Hybrid HVDC system for offshore wind farms connection using series-connected diode rectifier units," in *Proceedings of 2019 21st European Conference on Power Electronics and Applications*, Genova, Italy, Sept. 2019, pp. 1-10.
- [10] H. Gan, H. Xiao, Y. Huang *et al.*, "Cost-efficient hybrid converter for large-scale offshore wind power transmission," *IEEE Transactions on Power Delivery*, vol. 40, no. 3, pp. 1621-1633, Jun. 2025.
- [11] C. Wang, A. Ali, and F. Blaabjerg, "Composition and control of a new type of hybrid voltage-source converter based on DRUs and FB-MMC for large-scale offshore wind power integration and transmission," *IEEE Transactions on Power Electronics*, vol. 39, no. 5, pp. 5721-5732, May 2024.
- [12] L. Yu, S. Miao, J. Zhu *et al.*, "Self-synchronization control of offshore wind turbines connected with DRU-HVDC," *CSEE Journal of Power and Energy Systems*, doi: 10.17775/CSEEJPES.2022.03690
- [13] Y. Chang and X. Cai, "Hybrid topology of a diode-rectifier-based HVDC system for offshore wind farms," *IEEE Journal of Emerging and Selected Topics in Power Electronics*, vol. 7, no. 3, pp. 2116-2128, Sept. 2019.
- [14] B. Teng, J. Ma, and M. Zhu, "Diode-rectifier-based offshore platform for wind power collection and HVDC transmission system: implementation and hierarchical control," *IEEE Transactions on Sustainable Energy*, vol. 16, no. 2, pp. 812-825, Apr. 2025.
- [15] Y. Tang, Z. Zhang, and Z. Xu, "DRU based low frequency AC transmission scheme for offshore wind farm integration," *IEEE Transactions on Sustainable Energy*, vol. 12, no. 3, pp. 1512-1524, Jul. 2021.
- [16] R. Blasco-Gimenez, S. Añó-Villalba, J. Rodríguez-D'Erle *et al.*, "Distributed voltage and frequency control of offshore wind farms connected with a diode-based HVdc link," *IEEE Transactions on Power Electronics*, vol. 25, no. 12, pp. 3095-3105, Dec. 2010.
- [17] R. Blasco-Gimenez, S. Añó-Villalba, J. Rodríguez-D'Erle *et al.*, "Distributed voltage and frequency control of off-shore wind farms connected with a diode based HVDC link," in *Proceedings of 2010 36th Annual Conference on IEEE Industrial Electronics Society*, Glendale, USA, Nov. 2010, pp. 2994-2999.
- [18] C. Prignitz, H. G. Eckel, S. Achenbach *et al.*, "FixReF: a control strategy for offshore wind farms with different wind turbine types and diode rectifier HVDC transmission," in *Proceedings of 2016 IEEE 7th International Symposium on Power Electronics for Distributed Generation Systems*, Vancouver, Canada, Jun. 2016, pp. 1-7.
- [19] C. Prignitz, H. G. Eckel, and A. Rafoth, "FixReF sinusoidal control in line side converters for offshore wind power generation," in *Proceedings of 2015 IEEE 6th International Symposium on Power Electronics for Distributed Generation Systems*, Aachen, Germany, Jun. 2015, pp. 1-5.
- [20] K. Wang, Q. Song, B. Zhao *et al.*, "Grid-forming control of offshore wind farms connected with diode-based HVdc links based on remote active power regulation," *IEEE Transactions on Sustainable Energy*, vol. 15, no. 2, pp. 1315-1327, Apr. 2024.
- [21] L. Yu, R. Li and L. Xu, "Distributed PLL-based control of offshore wind turbines connected with diode-rectifier-based HVDC systems," *IEEE Transactions on Power Delivery*, vol. 33, no. 3, pp. 1328-1336, Jun. 2018.
- [22] R. Li, L. Yu, and L. Xu, "Operation of offshore wind farms connected with DRU-HVDC transmission systems with special consideration of faults," *Global Energy Interconnection*, vol. 1, no. 5, pp. 608-617, Dec. 2018.
- [23] L. Yu, L. Xu, J. Zhu *et al.*, "Impedance modelling and stability analysis of diode-rectifier based HVDC connected offshore wind farms," *IEEE Transactions on Power Delivery*, vol. 37, no. 1, pp. 591-602, Feb. 2022.
- [24] L. Yu, R. Li, L. Xu *et al.*, "Analysis and control of offshore wind farms connected with diode rectifier-based HVDC system," *IEEE Transactions on Power Delivery*, vol. 35, no. 4, pp. 2049-2059, Aug. 2020.
- [25] D. Yang, X. Wang, F. Liu *et al.*, "Symmetrical PLL for SISO impedance modeling and enhanced stability in weak grids," *IEEE Transactions on Power Electronics*, vol. 35, no. 2, pp. 1473-1483, Feb. 2020.
- [26] M. Á. Cardiel-Álvarez, S. Arnaltes, J. L. Rodríguez-Amenedo *et al.*, "Decentralized control of offshore wind farms connected to diode-based HVdc links," *IEEE Transactions on Energy Conversion*, vol. 33, no. 3, pp. 1233-1241, Sept. 2018.
- [27] H. Xiao, X. Huang, Y. Huang *et al.*, "Self-synchronizing control and frequency response of offshore wind farms connected to diode rectifier based HVDC system," *IEEE Transactions on Sustainable Energy*, vol. 13, no. 3, pp. 1681-1692, Jul. 2022.
- [28] Z. Zhang and X. Zhao, "Startup control of grid-forming offshore wind turbines connected to the diode-rectifier-based HVDC link," *IEEE Transactions on Sustainable Energy*, vol. 16, no. 1, pp. 407-418, Jan. 2025.
- [29] Y. Sun, D. Kong, Z. Zhang *et al.*, "Consensus-based distributed control of offshore wind farms connected via DR-HVDC," *IEEE Transactions on Industrial Electronics*, vol. 72, no. 6, pp. 5936-5947, Jun. 2025.
- [30] G. Zhang, W. Xiang, X. Chen *et al.*, "Grid-forming control based on adaptive reactive power allocation for offshore wind farms connected to diode-rectifier-based HVDC system," *Journal of Modern Power Systems and Clean Energy*, vol. 13, no. 1, pp. 154-166, Jan. 2025.
- [31] Z. Zhang, Y. Jin, and Z. Xu, "Grid-forming control of wind turbines for diode rectifier unit based offshore wind farm integration," *IEEE Transactions on Power Delivery*, vol. 38, no. 2, pp. 1341-1352, Apr. 2023.
- [32] H. Xiao, X. Huang, Y. Huang *et al.*, "Black start strategy of DRU-based low-frequency AC transmission system for offshore wind power integration," *IEEE Transactions on Industry Applications*, vol. 60, no. 6, pp. 8319-8328, Nov.-Dec. 2024.
- [33] Y. Li, X. Yuan, J. Li *et al.*, "Novel grid-forming control of PMSG-based wind turbine for integrating weak AC grid without sacrificing maximum power point tracking," *IET Generation, Transmission & Distribution*, vol. 15, no. 10, pp. 1613-1625, May 2021.
- [34] S. Wang, J. Hu, and X. Yuan, "Virtual synchronous control for grid-connected DFIG-based wind turbines," *IEEE Journal of Emerging and Selected Topics in Power Electronics*, vol. 3, no. 4, pp. 932-944, Dec. 2015.
- [35] Muhammad H. Rashid, *Power Electronics Handbook*, 4th ed. Oxford: Butterworth-Heinemann Ltd., 2018, pp. 177-208.
- [36] S. Cai and H. Wen, "Modeling and MPPT control of DFIG wind energy system," in *Proceedings of International Conference on Renewable Power Generation*, Beijing, China, Oct. 2015, pp. 1-6.
- [37] H. Nian and Y. Jiao, "Improved virtual synchronous generator control of DFIG to ride-through symmetrical voltage fault," *IEEE Transactions on Energy Conversion*, vol. 35, no. 2, pp. 672-683, Jun. 2020.
- [38] Q. Huang, X. Zou, D. Zhu *et al.*, "Scaled current tracking control for doubly fed induction generator to ride-through serious grid faults," *IEEE Transactions on Power Electronics*, vol. 31, no. 3, pp. 2150-2165, Mar. 2016.
- [39] R. Zhu, Z. Chen, Y. Tang *et al.*, "Dual-loop control strategy for DFIG-based wind turbines under grid voltage disturbances," *IEEE Transactions on Power Electronics*, vol. 31, no. 3, pp. 2239-2253, Mar. 2016.
- [40] H. Wu, H. Xu, Z. Li *et al.*, "Reactive current distribution strategy of DFIG's RSC and GSC considering electromagnetic stress and grid codes requirement," *IEEE Transactions on Energy Conversion*, vol. 38, no. 1, pp. 273-283, Mar. 2023.

Han Wu received the B.Eng. and M.Sc. degrees in electrical engineering from China University of Petroleum (East China), Qingdao, China, in 2020 and 2023, respectively. He is currently working toward the Ph.D. degree in electrical engineering with Zhejiang University, Hangzhou, China. His current research interests include control and stability analysis of wind power generation systems.

Tao Wang received the B.Eng. and Ph.D. degrees both from the College of Electrical Engineering, Zhejiang University, Hangzhou, China, in 2013 and 2018, respectively. From 2018 to 2020, he worked as a Postdoc Research Associate in the Electronic and Electrical Engineering Department of the University of Sheffield, Sheffield, U.K.. From 2020 to 2023, he was with Nanjing University of Aeronautics and Astronautics, Nanjing, China, where he worked as an Associate Professor in the College of Automation Engineering. Since 2024, he has been a Research Professor with the College of Electrical Engineering, Zhejiang University. His current research interests include wind power generation, aviation power supply, control of permanent magnet synchronous machine, and model predictive control.

Xiang Meng received the B.S., M.S., and Ph.D. degrees in electrical engi-

neering from Southwest Jiaotong University, Chengdu, China, in 2016, 2019, and 2023, respectively. He is currently a Postdoctoral Research Fellow with the College of Electrical Engineering, Zhejiang University, Hangzhou, China. His research interests include energy management and optimal control of on-board DC microgrid and traction motor control.

Lijian Wu received the B.Eng. and M.Sc. degrees from Hefei University of Technology, Hefei, China, in 2001 and 2004, respectively, and the Ph.D. degree from the University of Sheffield, Sheffield, U.K., in 2011, all in electri-

cal engineering. From 2004 to 2007, he was an Engineer with Delta Electronics Co., Ltd., Shanghai, China. From 2012 to 2013, he was with Sheffield Siemens Wind Power Research Center, sheffield, U.K., as a Design Engineer focusing on wind power generators. From 2013 to 2016, he was an Advanced Engineer with Siemens Wind Power A/S, Brande, Denmark. Since 2016, he has been with Zhejiang University, Hangzhou, China, where he is currently a Professor of electrical machines and control systems. His current research interests include design and control of permanent magnet synchronous machine.